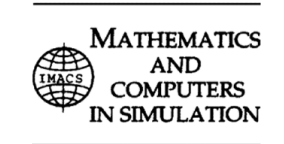




#### Available online at www.sciencedirect.com

# **ScienceDirect**



Mathematics and Computers in Simulation 177 (2020) 385-403

www.elsevier.com/locate/matcom

# Original articles

# Parameter-robust multiphysics algorithms for Biot model with application in brain edema simulation

Guoliang Ju<sup>a,1</sup>, Mingchao Cai<sup>b,\*,2</sup>, Jingzhi Li<sup>c,1</sup>, Jing Tian<sup>d</sup>

<sup>a</sup> School of Mechatronics Engineering, Harbin Institute of Technology, Harbin, Heilongjiang 150001, China
 <sup>b</sup> Department of Mathematics, Morgan State University, Baltimore, MD 21251, USA
 <sup>c</sup> Department of Mathematics, Southern University of Science and Technology, Shenzhen, Guangdong 518055, China
 <sup>d</sup> Department of Mathematics, Towson University, Towson, MD 21252, USA

Received 23 October 2019; received in revised form 26 February 2020; accepted 27 April 2020 Available online 4 May 2020

#### Abstract

In this paper, we develop parameter-robust numerical algorithms for Biot model and apply the algorithms in brain edema simulations. By introducing an intermediate variable, we derive a multiphysics reformulation of the Biot model. Based on the reformulation, the Biot model is viewed as a generalized Stokes subproblem combining with a reaction—diffusion subproblem. Solving the two subproblems together or separately leads to a coupled or a decoupled algorithm. We conduct extensive numerical experiments to show that the two algorithms are robust with respect to the key physical parameters. The algorithms are applied to study the brain swelling caused by abnormal accumulation of cerebrospinal fluid in injured areas. The effects of the key physical parameters on brain swelling are carefully investigated. It is observed that the permeability has the biggest influence on intracranial pressure (ICP) and tissue deformation; the Young's modulus and the Poisson ratio do not affect the maximum value of ICP too much but have big influence on the tissue deformation and the developing speed of brain swelling.

© 2020 International Association for Mathematics and Computers in Simulation (IMACS). Published by Elsevier B.V. All rights reserved.

Keywords: Biot equations; Poroelasticity; Brain edema

#### 1. Introduction

Brain swelling, usually including a pathologically increased intracranial pressure (ICP), can occur in specific locations or throughout the brain. High ICP will prevent blood from flowing to brain, which deprives it of the oxygen that needs to function. Brain swelling can also block other fluids from leaving brains, making the swelling even worse. It might even lead to the damage or death of brain cells. Roughly speaking, brain edema is an abnormal accumulation of cerebrospinal fluid (CSF) in the intracellular or extracellular space of the brain [1,2,26–29,41,46].

E-mail addresses: 11649009@mail.sustc.edu.cn (G. Ju), Mingchao.Cai@morgan.edu (M. Cai), li.jz@sustc.edu.cn (J. Li), jtian@towson.edu (J. Tian).

0378-4754/© 2020 International Association for Mathematics and Computers in Simulation (IMACS). Published by Elsevier B.V. All rights reserved.

<sup>\*</sup> Corresponding author.

<sup>&</sup>lt;sup>1</sup> This author's work is supported in part by the NSF of China under the grant No. 11571161 and 11731006, the Shenzhen Sci-Tech Fund No. JCYJ20160530184212170 and JCYJ20170818153840322.

<sup>&</sup>lt;sup>2</sup> This author's work is supported in part by NIH BUILD grant (ASCEND pilot project) through UL1GM118973, NSF HBCU-UP Research Initiation Award through HRD1700328 and NSF HBCU-UP Excellence in Research Award through DMS1831950.

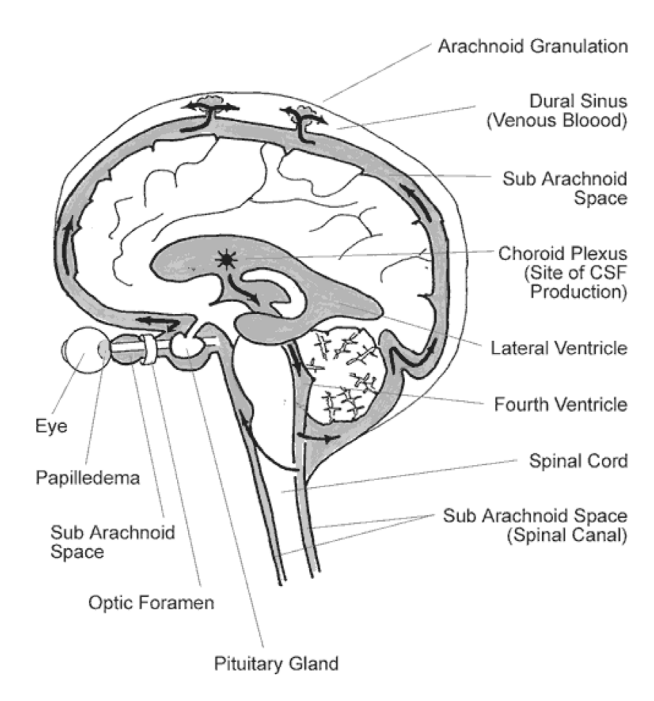


**Fig. 1.** The ventricles and CSF Flow. *Source:* From [2].

As studied by Hakim et al. [17], human brains consist of brain parenchyma and CSF. For illustration, Fig. 1 gives the circulation of CSF. CSF is produced by choroid plexus in ventricle and discharged in three ways: (i) most of it flows through the aqueduct, (ii) little of it flows across the ventricle wall into the parenchyma, (iii) some of it may flow through shunt. The ways (i) and (ii) make CSF flow around the subarachnoid space (SAS) part and be absorbed by arachnoid granulations in the SAS part. When traumatic brain injury (TBI) occurs, the brain tissues begin to absorb CSF. Recent works [25–27,33–35,46] indicate that poroelastic theory may provide a suitable mathematical model for the mechanical process of brain edema. By assuming that brain tissue is a poroelastic material, the process can be characterized by Biot's consolidation model, which describes the deformation of porous material containing viscous fluids [4,5].

There have been some numerical methods for solving the Biot model in poroelasticity. For example, Finite volume methods [36], mixed Finite Element methods [10,21,22,31,32,48,51], Galerkin least square methods [20], and combinations of different methods [39,47]. The major numerical difficulties are elasticity locking and pressure oscillation [10,19,22,38,49,50]. Elasticity locking is observed when the Poisson ratio is approaching 0.5, while pressure oscillations occur due to the Finite Element spaces are not compatible [49]. "Compatible" means that the Finite Element spaces need to satisfy certain inf-sup condition. In some recent numerical methods [38,47,49], to overcome the difficulties, mixed Finite Elements for linear elasticity operator and compatible Finite Element spaces for displacement and pressure are used. In this work, inspired by [13,23,37], we introduce an intermediate variable, called a "total pressure", and reformulate the Biot model into a 3-by-3 saddle point problem. By using such a multiphysics reformulation, we are able to view the Biot model as a combination of a generalized Stokes model (or a mixed form of linear elasticity) and a reaction-diffusion model for the fluid pressure. Such a reformulation naturally enables us to overcome the numerical difficulties caused by the elasticity locking and pressure oscillation. Based on the reformulation, we then design two algorithms: in the first algorithm, the generalized Stokes model and the reaction-diffusion model are solved together which leads to a coupled algorithm; in the second algorithm, the generalized Stokes problem is solved using the previous time-step solution of the fluid pressure as the righthand side, and then the reaction-diffusion problem is solved by using the most updated solution of the generalized Stokes subproblem. The second algorithm is actually a decoupled algorithm. The advantages of the multiphysics reformulation based algorithms are as follows: firstly, the reformulation enables us to use the classical inf-sup

stable Finite Elements for Stokes problem [6] and traditional Lagrange elements for the parabolic type reaction—diffusion equation. Thus, sophisticated discretization is avoided. Secondly, no matter the coupled algorithm or the decoupled algorithm is used, some existing fast solvers like Multigrid [8,16,45] or domain decomposition methods [9,12] for the generalized Stokes operator and the reaction—diffusion operator can be naturally incorporated in. We would emphasize that our algorithms are parameter-robust, which is a very important feature for both biomedical applications and geomechanical applications.

In biomechanical simulations, challenges come from many aspects, for example, mathematical modeling, boundary conditions, force term, source terms, and material properties. For brain swelling simulations, the most difficult part is from the material properties of brain tissue. There have been big variations in the poroelastic constants used. Regarding the specific storage term,  $c_0$ , most previous studies implicitly ignore it in steady-state models, considering that the interstitial fluid and cerebral cells are completely incompressible [30]. A Poisson ratio of  $\nu = 0.35$  is the most commonly used value when modeling brain tissue in clinical applications [41], however, a much higher value of  $\nu = 0.496$  was derived from experiments [14] (or an almost value of 0.5 is used in [42]). In the literature, other relevant parameters variations for modeling brain edema include: Young's modulus ranges from 584 Pa [43] to  $10^4$  Pa [28], and the permeability [25] ranges from  $10^{-14}$  m<sup>2</sup> to  $10^{-16}$  m<sup>2</sup>. Thus, numerical methods which are robust for model parameters become an essential factor of brain swelling simulation. Moreover, it is very important to study the behavioral characteristics of brain material in detail so that numerical simulations can provide useful information for brain swelling treatments. The goal of our work is to apply the developed algorithms to study the ICP and the deformation of brain parenchyma, and identify the effects of the key parameters on brain swelling. For our algorithms, we firstly demonstrate that they converge in optimal orders and are parameter-robust. Then, we apply them into brain swelling simulation. The numerical results show good agreements with existing published works, which further validate the effectiveness of our algorithms.

The rest of this paper is organized as follows. In Section 2, we present the PDE model, its multiphysics reformulation, the corresponding variational forms, and the numerical algorithms. In Section 3, we validate the numerical algorithms by testing their robustness with respect to different physical parameters. We apply our algorithms to investigate the effects of the key parameters on brain swelling in Section 4. The limitations and possibilities of improving of our numerical study are also discussed. Conclusions are drawn in Section 5.

#### 2. The PDE model and the numerical algorithms

The most frequently used poroelastic model in various applications is the following quasi-static Biot model:

$$-\operatorname{div}\sigma(\boldsymbol{u}) + \alpha \nabla p = f, \tag{1}$$

$$(c_0 p + \alpha \operatorname{div} \mathbf{u})_t - \operatorname{div} K \left( \nabla p - \rho_f \mathbf{g} \right) = Q_s. \tag{2}$$

Eq. (1) describes the force equilibrium for the solid phase. Eq. (2) describes the conservation of mass for the fluid phase. Inherently, because of the pore structure, the filtration velocity of fluid  $v_f$  satisfies Darcy's law:

$$\mathbf{v}_f := -K \left( \nabla p - \rho_f \mathbf{g} \right). \tag{3}$$

In the model, u denotes the displacement vector of the solid phase, p denotes the pressure of the fluid phase, f is the body force,  $Q_s$  is a source or sink term,  $\rho_f$  is the fluid density, g is the gravitational acceleration,  $c_0 > 0$  is the constrained specific storage coefficient,  $\alpha$  is the Biot-Willis constant which is close to 1,  $K = \kappa/\mu_f$  is the hydraulic conductivity with  $\kappa > 0$  being the permeability and  $\mu_f$  being the fluid viscosity.

$$\sigma(\boldsymbol{u}) := 2\mu\varepsilon(\boldsymbol{u}) + \lambda \mathrm{div}\boldsymbol{u} \ \mathbf{I}, \quad \varepsilon(\boldsymbol{u}) := \frac{1}{2} \left( \nabla \boldsymbol{u} + \nabla \boldsymbol{u}^T \right),$$

where  $\lambda$  and  $\mu$  are Lamé constants which can be computed by using the Young's modulus E and the Poisson ratio  $\nu$ :

$$\lambda = \frac{E\nu}{(1+\nu)(1-2\nu)} \quad \text{and} \quad \mu = \frac{E}{2(1+\nu)}.$$

In (2),  $Q_s$  makes the liquid flows into the solid and causes the dilation of the solid skeleton, and  $c_0p + \alpha \operatorname{div} \boldsymbol{u}$  describes the fluid mass increment that caused by either the dilation of the solid skeleton or the compressibility of fluids in the pores due to pressure changes. The physical meanings of mathematical symbols are listed in Table 1.

	<u> </u>	1 617	
Syms	Physics meaning	Syms	Physics meaning
p	Fluid pressure	E	Young's modulus
ν	Poisson ratio	α	Biot coefficient (of effective stress)
$c_0$	Specific storage term	κ	Permeability of the brain
$\mu_f$	Fluid viscosity	$Q_s$	Source or sink term
u	Displacement	n	Normal vector
$v_f$	Fluid velocity	$\lambda, \mu$	Lamé constants

Table 1
Lists of the main mathematical symbols and the corresponding physics meanings.

To close the above system, suitable boundary and initial conditions must be prescribed. For the ease of presentation and without loss of generality, we consider mixed partial Neumann and partial Dirichlet boundary conditions in this paper. Specifically, the boundaries for  $\boldsymbol{u}$  and  $\boldsymbol{p}$  are divided into

$$\partial \Omega = \Gamma_d \cup \Gamma_t$$
 and  $\partial \Omega = \Gamma_p \cup \Gamma_f$ .

Here,  $\Gamma_d$  and  $\Gamma_t$  are the Dirichlet boundary and the Neumann boundary for  $\boldsymbol{u}$  respectively;  $\Gamma_p$  and  $\Gamma_f$  are the Dirichlet boundary and the Neumann boundary for p respectively. We assume that the Lebesgue measures of  $\Gamma_d$  and  $\Gamma_p$  are positive. The boundary conditions are

$$\begin{cases}
 u = 0 & \text{on } \Gamma_d, \\
 \sigma(u)n - \alpha p n = h & \text{on } \Gamma_t, \\
 p = 0 & \text{on } \Gamma_p, \\
 K(\nabla p - \rho_f \mathbf{g}) \cdot \mathbf{n} = g_2 & \text{on } \Gamma_f.
\end{cases} \tag{4}$$

Without loss of generality, the Dirichlet boundary conditions in (4) are assumed to be homogeneous. The initial conditions are:

$$u(0) = u_0$$
 and  $p(0) = p_0$ . (5)

To study the weak solution of the Biot model, we introduce the following functional spaces.

$$V := \{ \mathbf{v} \in \mathbf{H}^1(\Omega); \ \mathbf{v}|_{\Gamma_d} = 0 \},$$
  
$$M := \{ \psi \in H^1(\Omega); \ \psi|_{\Gamma_p} = 0 \}.$$

Their dual spaces are denoted as V' and M'. We use  $(\cdot, \cdot)$  and  $(\cdot, \cdot)$  to denote the  $L^2$ - inner products on  $\Omega$  and on boundary respectively. Moreover, let us make the following assumption.

**Assumption 1.** We assume that  $u_0 \in H^1(\Omega)$ ,  $f \in L^2(\Omega)$ ,  $h \in L^2(\Gamma_t)$ ,  $p_0 \in L^2(\Omega)$ ,  $Q_s \in L^2(\Omega)$ ,  $g_2 \in L^2(\Gamma_f)$ ,  $\mu \in (0, +\infty)$ ,  $\lambda \in [1, +\infty)$ , K is positive and has uniform lower and upper bounds,  $c_0 \ge 0$ , and T > 0.

The variational problem for (1)–(2) with the boundary conditions (4) read as: find a tuple (u, p) with

$$\mathbf{u} \in L^{\infty}(0, T; \mathbf{V}), \ p \in L^{\infty}(0, T; L^{2}(\Omega)) \cap L^{2}(0, T; M),$$
  
 $p_{t}, (\text{div}\mathbf{u})_{t} \in L^{2}(0, T; M'),$ 

such that (u, p) satisfies the initial conditions (5) and

$$2\mu \left(\varepsilon(\boldsymbol{u}), \varepsilon(\boldsymbol{v})\right) + \lambda \left(\operatorname{div}\boldsymbol{u}, \operatorname{div}\boldsymbol{v}\right) - \alpha \left(p, \operatorname{div}\boldsymbol{v}\right) = (\boldsymbol{f}, \boldsymbol{v}) + \langle \boldsymbol{h}, \boldsymbol{v} \rangle_{\Gamma_t}, \quad \forall \boldsymbol{v} \in \boldsymbol{V}, \tag{6}$$

$$((c_0 p + \alpha \operatorname{div} \mathbf{u})_t, \psi) + K (\nabla p - \rho_f \mathbf{g}, \nabla \psi) = (Q_s, \psi) + \langle g_2, \psi \rangle_{\Gamma_f}, \quad \forall \psi \in M,$$
(7)

for almost every  $t \in (0, T]$ . The derivation of the above weak form is based on integration by parts. For the justification of the well-posedness of the weak problem (6)–(7), one can endow  $V \times M$  a weighted norm:

$$\|(\boldsymbol{u}, p)\|^2 := 2\mu \|\boldsymbol{u}\|_1^2 + \lambda \|\operatorname{div}\boldsymbol{u}\|_0^2 + c_0 \|p\|_0^2 + K \|\nabla p\|_0^2$$

and prove that the corresponding linear operator induced by (6)–(7) is an isomorphism from  $V \times M$  to its dual space. However, the drawback of using such a formulation is that there is no parameter robust solver for the graddiv dominant term as  $\lambda \to +\infty$  [23]. We refer the readers to [23] or [13] for the details of discussions.

Unlike those conventional methods which directly approximate the original model (1)–(2), we adopt a multiphysics reformulation method in this paper. Note that  $\lambda$  and  $\mu$  are constants, there holds the following identity.

$$-\operatorname{div}\left(\mu[\nabla \boldsymbol{u} + \nabla \boldsymbol{u}^T]\right) - \nabla\lambda\operatorname{div}\boldsymbol{u} = -\mu\boldsymbol{\Delta}\boldsymbol{u} - (\mu + \lambda)\,\nabla\operatorname{div}\boldsymbol{u}.$$

If we introduce a new variable

$$\xi = \alpha p - \lambda \operatorname{div} \mathbf{u},\tag{8}$$

then problem (1)–(2) can be reformulated as:

$$-2\mu \operatorname{div}\left(\varepsilon(\boldsymbol{u})\right) + \nabla \xi = \boldsymbol{f},\tag{9}$$

$$-\operatorname{div}\boldsymbol{u} - \frac{1}{\lambda}\boldsymbol{\xi} + \frac{\alpha}{\lambda}\boldsymbol{p} = 0,\tag{10}$$

$$\left(\left(c_0 + \frac{\alpha^2}{\lambda}\right)p - \frac{\alpha}{\lambda}\xi\right)_t - K\operatorname{div}\left(\nabla p - \rho_f \mathbf{g}\right) = Q_s. \tag{11}$$

After the reformulation, the boundary conditions (4) and initial conditions (5) can still be applied to the problem (9)–(11). We comment here that  $\xi$  can be called a "total pressure". To complete the system, the only information needed is the initial condition  $\xi$ (0), which can be derived by using (8). Moreover, from (8), if  $\xi$  and u are obtained, one can recover p by

$$p = \frac{1}{\alpha} \left( \xi + \lambda \operatorname{div} \boldsymbol{u} \right).$$

Based on (9)–(11), the proper functional spaces for the primary variables are:  $u \in V, \xi \in W = L^2(\Omega)$ , and  $p \in M$ . If we move  $\frac{\alpha}{\lambda}p$  to the right-hand side of (10), the equation becomes

$$-\operatorname{div}\boldsymbol{u} - \frac{1}{\lambda}\boldsymbol{\xi} = -\frac{\alpha}{\lambda}p. \tag{12}$$

Combining (9) with Eq. (12), we obtain the generalized Stokes (or the mixed form of the linear elasticity) equations for u and  $\xi$ . To simplify the presentation, henceforth, we will assume that g = 0. Moreover, we assume that  $u_0, f, h, p_0, \phi, g_2$ , and the model parameters satisfy Assumption 1.

Given T > 0, a 3-tuple  $(\boldsymbol{u}, \boldsymbol{\xi}, p) \in \boldsymbol{X} = \boldsymbol{V} \times \boldsymbol{W} \times \boldsymbol{M}$  with

$$u \in L^{\infty}(0, T; V), \xi \in L^{\infty}(0, T; W),$$
  
 $p \in L^{\infty}(0, T; L^{2}(\Omega)) \cap L^{2}(0, T; M),$   
 $p_{t}, \xi_{t} \in L^{2}(0, T; M'),$ 

is called a weak solution of (9)–(11), if there holds for almost every  $t \in (0, T]$ 

$$2\mu \left(\varepsilon(\boldsymbol{u}), \varepsilon(\boldsymbol{v})\right) - \left(\xi, \operatorname{div}\boldsymbol{v}\right) = (\boldsymbol{f}, \boldsymbol{v}) + \langle \boldsymbol{h}, \boldsymbol{v} \rangle_{\Gamma_t}, \quad \forall \boldsymbol{v} \in \boldsymbol{V}, \tag{13}$$

$$-\left(\operatorname{div}\boldsymbol{u},\phi\right) - \frac{1}{\lambda}\left(\xi,\phi\right) + \frac{\alpha}{\lambda}\left(p,\phi\right) = 0, \quad \forall \phi \in W,\tag{14}$$

$$\left(\left(\left(c_0 + \frac{\alpha^2}{\lambda}\right)p - \frac{\alpha}{\lambda}\xi\right)_t, \psi\right) + K\left(\nabla p, \nabla \psi\right) = (Q_s, \psi) + K\langle g_2, \psi\rangle_{\Gamma_f}, \quad \forall \psi \in M.$$
(15)

We assume that a backward Euler scheme is applied to (15). For discussing the well-posedness and parameter-robust solvers for the resulting linear system, one needs to introduce the following norms:

$$(2\mu \|\boldsymbol{\epsilon}(\boldsymbol{u})\|_0^2)^{\frac{1}{2}}, \quad \left(\frac{1}{\lambda} \|\boldsymbol{\xi}\|_0^2\right)^{\frac{1}{2}}, \quad \left(\left(c_0 + \frac{\alpha^2}{\lambda}\right) \|p\|_0^2 + \Delta t K \|\nabla p\|_0^2\right)^{\frac{1}{2}}$$

for the functional spaces  $V \times W \times M$ . The corresponding inf-sup condition

$$\inf_{(\boldsymbol{u},\xi,p)} \sup_{(\boldsymbol{v},\phi,\psi)} \frac{(\mathcal{A}(\boldsymbol{u},\xi,p),(\boldsymbol{v},\phi,\psi))}{\|(\boldsymbol{u},\xi,p)\|_X \|(\boldsymbol{v},\phi,\psi)\|_X} \ge \beta > 0$$

holds uniformly independent of model parameters (specifically,  $\mu$ ,  $\lambda$ ,  $c_0 + \frac{\alpha^2}{\lambda}$ , and  $\Delta t K$ ). Here,  $\mathcal{A}$  is the linear operator induced by the whole coupled problem. The proof can be derived in a similar way as that in Theorem 3.2 of [23].

As (9)–(10) is the generalized Stokes problem, we apply the Taylor–Hood elements, i.e.,  $(P_2, P_1)$  Lagrange finite elements for the pair  $(u, \xi)$ . Eq. (11) is a reaction–diffusion problem for the fluid pressure.  $P_1$  Lagrange finite elements are adopted for the discretization. That is,

$$V_{h} := \{ \mathbf{v}_{h} \in \mathbf{C}^{0}(\bar{\Omega}); \ \mathbf{v}_{h}|_{\Gamma_{d}} = 0, \ \mathbf{v}_{h}|_{K} \in \mathbf{P}_{2}(K), \ \forall K \in T_{h} \},$$

$$W_{h} := \{ \phi_{h} \in C^{0}(\bar{\Omega}); \phi_{h}|_{K} \in P_{1}(K), \ \forall K \in T_{h} \},$$

$$M_{h} := \{ \psi_{h} \in C^{0}(\bar{\Omega}); \ \psi|_{\Gamma_{n}} = 0, \ \psi_{h}|_{K} \in P_{1}(K), \ \forall K \in T_{h} \}.$$
(16)

In addition, we require that the Finite element spaces are conforming, i.e.,  $V_h \subset V$ ,  $M_h \subset M$  and  $W_h \subset W$ .

For the time discretization, we apply a backward Euler scheme. If all the three unknowns are solved together based on (9)–(11), then the resulting algorithm is a coupled method, which is described in Algorithm 1.

# Algorithm 1 A Coupled Algorithm

Input: Evaluate 
$$\boldsymbol{u}_{h}^{0} \in V_{h}$$
,  $p_{h}^{0} \in M_{h}$ , and  $\xi_{h}^{0} \in W_{h}$  by  $\xi_{h}^{0} = \alpha p_{h}^{0} - \lambda \operatorname{div} \boldsymbol{u}_{h}^{0}$ .

for  $n = 0, 1, 2, \dots$  do

Solve for  $(\boldsymbol{u}_{h}^{n+1}, \xi_{h}^{n+1}, p_{h}^{n+1}) \in V_{h} \times W_{h} \times M_{h}$  such that:

$$2\mu \left(\varepsilon(\boldsymbol{u}_{h}^{n+1}, \varepsilon(\boldsymbol{v}_{h})) - \left(\xi_{h}^{n+1}, \operatorname{div} \boldsymbol{v}_{h}\right) = (\boldsymbol{f}, \boldsymbol{v}_{h}) + \langle \boldsymbol{h}, \boldsymbol{v}_{h} \rangle_{\Gamma_{t}}, \ \forall \boldsymbol{v}_{h} \in V_{h}, \\ -\left(\operatorname{div} \boldsymbol{u}_{h}^{n+1}, \phi_{h}\right) - \frac{1}{\lambda} \left(\xi_{h}^{n+1}, \phi_{h}\right) + \frac{1}{\lambda} \left(\alpha p_{h}^{n+1}, \phi_{h}\right) = 0, \quad \forall \phi_{h} \in W_{h}, \\ \left(\left(\left(c_{0} + \frac{\alpha^{2}}{\lambda}\right) p_{h}^{n+1} - \frac{\alpha}{\lambda} \xi_{h}^{n+1}\right) / \Delta t, \psi_{h}\right) + K \left(\nabla p_{h}^{n+1}, \nabla \psi_{h}\right) = (Q_{s}, \psi_{h}) \\ + \left(\left(\left(c_{0} + \frac{\alpha^{2}}{\lambda}\right) p_{h}^{n} - \frac{\alpha}{\lambda} \xi_{h}^{n}\right) / \Delta t, \psi_{h}\right) + \langle g_{2}, \psi_{h} \rangle_{\Gamma_{f}}, \ \forall \psi_{h} \in M_{h}.$$

# end for

As previously observed, combining (9) and (12), we obtain a mixed form of the linear elasticity (or a generalized Stokes) problem. One can solve such a problem for u and  $\xi$  by using the solution of p at the previous time-step. Then we solve the reaction–diffusion problem (11). The resulting algorithm is a decoupled algorithm and the details are listed in Algorithm 2. By "decoupled", we mean that the computations of the two subproblems can be realized separately.

#### 3. Benchmark tests

In this section, we present numerical experiments to show that the two algorithms are robust with respect to the physical parameters and the mesh refinements. All algorithms are implemented by using FreeFEM++ [18]. The code is available upon request. The benchmark model for accuracy test is from [49] while the coefficient setting and the boundary condition are slightly different (but will not affect the conclusions).

**Example 1.** Let  $\Omega = [0, 1] \times [0, 1]$  with  $\Gamma_1 = \{(1, y); 0 \le y \le 1\}$ ,  $\Gamma_2 = \{(x, 0); 0 \le x \le 1\}$ ,  $\Gamma_3 = \{(0, y); 0 \le y \le 1\}$ , and  $\Gamma_4 = \{(x, 1); 0 \le x \le 1\}$ . The normal vector of the boundary is denoted as  $\mathbf{n} = (n_1, n_2)^T$ . The final time is T = 0.001. The source term, the force term, the boundary conditions, and the initial conditions are as follows.

$$Q_{s} = e^{-t} \left( (-c_{0} + 2\pi^{2}K) \sin(\pi x) \sin(\pi y) - \frac{\alpha\pi}{\mu + \lambda} \sin(\pi(x + y)) \right),$$

$$f = e^{-t} \left( 4\mu\pi^{2} \sin(2\pi y)(2\cos(2\pi x) - 1) + \left( \frac{2\mu\pi^{2}}{\mu + \lambda} \sin(\pi x) + \alpha\pi \cos(\pi x) \right) \sin(\pi y) - \pi^{2} \cos(\pi(x + y)) \right),$$

$$4\mu\pi^{2} \sin(2\pi x)(1 - 2\cos(2\pi y)) + \left( \frac{2\mu\pi^{2}}{\mu + \lambda} \sin(\pi y) + \alpha\pi \cos(\pi y) \right) \sin(\pi x) - \pi^{2} \cos(\pi(x + y)) \right),$$

# Algorithm 2 A Decoupled Algorithm

**Input:** Evaluate  $\boldsymbol{u}_h^0 \in \boldsymbol{V}_h$ ,  $p_h^0 \in M_h$ , and  $\xi_h^0 \in W_h$  by  $\xi_h^0 = \alpha p_h^0 - \lambda \text{div} \boldsymbol{u}_h^0$ 

for  $n = 0, 1, 2, \dots$  do
(i) Finding  $(\boldsymbol{u}_h^{n+1}, \xi_h^{n+1}) \in V_h \times M_h$  such that:

$$2\mu\left(\varepsilon(\boldsymbol{u}_{h}^{n+1}),\varepsilon(\boldsymbol{v}_{h})\right) - \left(\xi_{h}^{n+1},\operatorname{div}\boldsymbol{v}_{h}\right) = (\boldsymbol{f},\boldsymbol{v}_{h}) + \langle \boldsymbol{h},\boldsymbol{v}_{h}\rangle_{\Gamma_{t}}, \ \forall \boldsymbol{v}_{h} \in \boldsymbol{V}_{h},$$
$$-\left(\operatorname{div}\boldsymbol{u}_{h}^{n+1},\phi_{h}\right) - \frac{1}{\lambda}\left(\xi_{h}^{n+1},\phi_{h}\right) = -\frac{1}{\lambda}\left(\alpha p_{h}^{n},\phi_{h}\right), \ \forall \phi_{h} \in W_{h}.$$

(ii) Using  $(\xi_h^{n+1}, p_h^n)$  obtained in i), solve for  $p_h^{n+1}$  by

$$\left(\left(c_{0} + \frac{\alpha^{2}}{\lambda}\right) \frac{p_{h}^{n+1}}{\Delta t}, \psi_{h}\right) + K\left(\nabla p_{h}^{n+1}, \nabla \psi_{h}\right) = (Q_{s}, \psi_{h}) + \left(\left(c_{0} + \frac{\alpha^{2}}{\lambda}\right) \frac{p_{h}^{n}}{\Delta t}, \psi_{h}\right) + \frac{\alpha}{\lambda} \left(\frac{\xi_{h}^{n+1} - \xi_{h}^{n}}{\Delta t}, \psi_{h}\right) + \langle g_{2}, \psi_{h} \rangle_{\Gamma_{f}}, \ \forall \psi_{h} \in M_{h}.$$

end for

$$p = e^{-t} \sin(\pi x) \sin(\pi y) \quad \text{on } \Gamma_j, \ j = 1, 3,$$

$$u_1 = e^{-t} \left( \sin(2\pi y)(\cos(2\pi x) - 1) + \frac{1}{\mu + \lambda} \sin(\pi x) \sin(\pi y) \right) \quad \text{on } \Gamma_j, \ j = 1, 3,$$

$$u_2 = e^{-t} \left( \sin(2\pi x)(1 - \cos(2\pi y)) + \frac{1}{\mu + \lambda} \sin(\pi x) \sin(\pi y) \right) \quad \text{on } \Gamma_j, \ j = 1, 3,$$

$$\sigma \mathbf{n} - \alpha p \mathbf{n} = \mathbf{h} \quad \text{on } \Gamma_j, \ j = 2, 4,$$

$$\nabla p \cdot \mathbf{n} = e^{-t} (\pi \cos(\pi x) \sin(\pi y) n_1 + \pi \sin(\pi x) \cos(\pi y) n_2) \quad \text{on } \Gamma_j, \ j = 2, 4,$$

$$\mathbf{u} = \begin{pmatrix} \sin(2\pi y)(\cos(2\pi x) - 1) + \frac{1}{\mu + \lambda} \sin(\pi x) \sin(\pi y) \\ \sin(2\pi x)(1 - \cos(2\pi y)) + \frac{1}{\mu + \lambda} \sin(\pi x) \sin(\pi y) \end{pmatrix}, \quad p = \sin(\pi x) \sin(\pi y) \quad \text{in } \Omega \times \{t = 0\},$$

$$(17)$$

where

$$\begin{split} h_1 &= \left(-4\mu\pi\sin(2\pi y)\sin(2\pi x) + \left(\frac{2\mu\pi}{\mu+\lambda}\cos(\pi x) - \alpha\sin(\pi x)\right)\sin(\pi y) \\ &+ \frac{\pi\lambda}{\mu+\lambda}\sin(\pi(x+y))\right)n_1e^{-t} + \left(2\mu\pi(\cos(2\pi x) - \cos(2\pi y)) + \frac{\mu\pi}{\mu+\lambda}\sin(\pi(x+y))\right)n_2e^{-t} \\ h_2 &= \left(2\mu\pi(\cos(2\pi x) - \cos(2\pi y)) + \frac{\mu\pi}{\mu+\lambda}\sin(\pi(x+y))\right)n_1e^{-t} + \left(\left(\frac{2\mu\pi}{\mu+\lambda}\cos(\pi y) - \alpha\sin(\pi y)\right) + 4\mu\pi\sin(2\pi x)\sin(2\pi y) + \sin(\pi x) + \frac{\pi\lambda}{\mu+\lambda}\sin(\pi(x+y))\right)n_2e^{-t} \end{split}$$

By using these data, the exact solution for problem (1)–(2) is

$$\mathbf{u} = e^{-t} \left( \begin{array}{c} \sin(2\pi y)(\cos(2\pi x) - 1) + \frac{1}{\mu + \lambda} \sin(\pi x) \sin(\pi y) \\ \sin(2\pi x)(1 - \cos(2\pi y)) + \frac{1}{\mu + \lambda} \sin(\pi x) \sin(\pi y) \end{array} \right), \quad p = e^{-t} \sin(\pi x) \sin(\pi y).$$

**Table 2** Rate of convergence of the coupled algorithm for v = 0.3.

1/h	$L^2 \& H^1$ errors of $\boldsymbol{u}$	Orders	$L^2 \& H^1$ errors of $\xi$	Orders	$L^2 \& H^1$ errors of $p$	Orders
16	2.031e-3 & 1.020e-1		9.185e-3 & 7.894e-1		1.220e-2 & 2.353e-1	
32	4.856e-4 & 2.571e-2	2.06 & 1.99	2.294e-3 & 3.915e-1	2.00 & 1.01	3.072e-3 & 1.113e-1	1.99 & 1.08
64	1.201e-4 & 6.445e-3	2.02 & 2.00	5.732e-4 & 1.953e-1	2.00 & 1.00	7.692e-4 & 5.477e-2	2.00 & 1.00
128	2.994e-5 & 1.613e-3	2.00 & 2.00	1.433e-4 & 9.762e-2	2.00 & 1.00	1.924e-4 & 2.727e-2	2.00 & 1.01

**Table 3** Rate of convergence of the coupled algorithm for v = 0.49999.

1/h	$L^2 \& H^1$ errors of $\boldsymbol{u}$	Orders	$L^2 \& H^1$ errors of $\xi$	Orders	$L^2 \& H^1$ errors of $p$	Orders
16	7.800e-4 & 1.008e-1		9.927e-3 & 1.277		3.957e-3 & 2.174e-1	
32	9.453e-5 & 2.541e-2	3.04 & 1.99	2.438e-3 & 0.635	2.03 & 1.01	9.917e-4 & 1.089e-1	2.00 & 1.00
64	1.171e-5 & 6.367e-3	3.01 & 2.00	6.070e-4 & 0.317	2.01 & 1.00	2.481e-4 & 5.446e-2	2.00 & 1.00
128	1.460e-6 & 1.593e-3	3.00 & 2.00	1.516e-4 & 0.159	2.00 & 1.00	6.202e-5 & 2.723e-2	2.00 & 1.00

**Table 4** Rate of convergence of the decoupled algorithm for v = 0.3.

1/h	$L^2 \& H^1$ errors of $\boldsymbol{u}$	Orders	$L^2\&H^1$ errors of $\xi$	Orders	$L^2 \& H^1$ errors of $p$	Orders
16	2.031e-3 & 1.020e-1		9.185e-3 & 7.894e-1		1.220e-2 & 2.353e-1	
32	4.855e-4 & 2.571e-2	2.06 & 1.99	2.294e-3 & 3.915e-1	2.00 & 1.01	3.072e-3 & 1.113e-1	1.99 & 1.08
64	1.201e-4 & 6.445e-3	2.02 & 2.00	5.731e-4 & 1.953e-1	2.00 & 1.00	7.692e-4 & 5.477e-2	2.00 & 1.00
128	2.991e-5 & 1.613e-3	2.00 & 2.00	1.432e-4 & 9.762e-2	2.00 & 1.00	1.923e-4 & 2.727e-2	2.00 & 1.01

**Table 5** Rate of convergence of the decoupled algorithm for  $\nu = 0.49999$ .

1/h	$L^2 \& H^1$ errors of $\boldsymbol{u}$	Orders	$L^2\&H^1$ errors of $\xi$	Orders	$L^2 \& H^1$ errors of $p$	Orders
16	7.800e-4 & 1.008e-1		9.927e-3 & 1.277		3.957e-3 & 2.174e-1	
32	9.453e-5 & 2.541e-2	3.04 & 1.99	2.438e-3 & 0.635	2.03 & 1.01	9.917e-4 & 1.089e-1	2.00 & 1.00
64	1.171e-5 & 6.367e-3	3.01 & 2.00	6.070e-4 & 0.317	2.01 & 1.00	2.481e-4 & 5.446e-2	2.00 & 1.00
128	1.460e-6 & 1.593e-3	3.00 & 2.00	1.516e-4 & 0.159	2.00 & 1.00	6.202e-5 & 2.723e-2	2.00 & 1.00

Note that the solution is designed to satisfy  $\operatorname{div} \boldsymbol{u} = \pi e^{-t} \sin(\pi(x+y))/(\mu+\lambda) \to 0$  as  $\lambda \to +\infty$  at any time t. As the key parameters are the Poisson ratio  $\nu$  and the diffusion coefficient K, others parameters including E are fixed to be 1.

#### 3.1. Tests for the parameter v

In this part, we test the robustness of the two algorithms with respect to the Poisson ratio  $\nu$ . We fix the hydraulic conductivity to be K=1 and the constrained specific storage coefficient to be  $c_0=1$ , while vary the Poisson ratio to be  $\nu=0.3$  or  $\nu=0.49999$ .

We firstly report the numerical results of the coupled algorithm. In Tables 2 and 3, we show the numerical errors and the convergence orders for the case  $\nu=0.3$  and  $\nu=0.49999$  separately. The time step size is set as  $\Delta t=1.0\times 10^{-5}$ , which is small so that the time error is not dominant. Uniform grid with initial space step h=1/16 is used. The mesh refinement is based on linking the midpoints of each triangle. From the numerical results, we observe that no matter  $\nu=0.49999$  or  $\nu=0.3$ , the  $H^1$  error orders of u, the u0 error orders of u2 error orders of u3 are all around 2. The u1 error orders of u3 are around 1. As we use Taylor–Hood elements for the pair u3 and u4 elements for u5, the numerical results exhibit optimal approximation orders in the energy norm.

To validate the decoupled algorithm, we report the numerical results in Tables 4 and 5 for the cases  $\nu = 0.3$  and  $\nu = 0.49999$  respectively. For the decoupled algorithm, we set  $\Delta t = 1.0 \times 10^{-6}$  which is small to ensure the

**Table 6** Rate of convergence of the coupled algorithm for  $K = 10^{-2}$ .

1/h	$L^2 \& H^1$ errors of $\boldsymbol{u}$	Orders	$L^2\&H^1$ errors of $\xi$	Orders	$L^2 \& H^1$ errors of $p$	Orders
16	2.119e-3 & 1.020e-1		9.406e-3 & 7.907e-1		1.265e-2 & 2.455e-1	
32	5.176e-4 & 2.572e-2	2.03 & 1.99	2.363e-3 & 3.919e-1	1.99 & 1.01	3.208e-3 & 1.151e-1	1.98 & 1.09
64	1.296e-4 & 6.448e-3	2.00 & 2.00	5.926e-4 & 1.954e-1	2.00 & 1.00	8.063e-4 & 5.581e-2	1.99 & 1.04
128	3.249e-5 & 1.614e-3	2.00 & 2.00	1.483e-4 & 9.764e-2	2.00 & 1.00	2.020e-4 & 2.748e-2	2.00 & 1.02

**Table 7** Rate of convergence of the coupled algorithm for  $K = 10^{-6}$ .

1/h	$L^2 \& H^1$ errors of $\boldsymbol{u}$	Orders	$L^2\&H^1$ errors of $\xi$	Orders	$L^2 \& H^1$ errors of $p$	Orders
16	2.120e-3 & 1.020e-1		9.409e-3 & 7.907e-1		1.266e-2 & 2.457e-1	
32	5.181e-4 & 2.572e-2	2.03 & 1.99	2.365e-3 & 3.919e-1	1.99 & 1.01	3.210e-3 & 1.153e-1	1.98 & 1.09
64	1.298e-4 & 6.448e-3	2.00 & 2.00	5.932e-4 & 1.955e-1	1.99 & 1.00	8.075e-4 & 5.598e-2	1.99 & 1.04
128	3.260e-5 & 1.614e-3	2.00 & 2.00	1.486e-4 & 9.765e-2	2.00 & 1.00	2.024e-4 & 2.760e-2	2.00 & 1.02

**Table 8** Rate of convergence of the decoupled algorithm for  $K = 10^{-2}$ .

1/h	$L^2 \& H^1$ errors of $\boldsymbol{u}$	Orders	$L^2\&H^1$ errors of $\xi$	Orders	$L^2 \& H^1$ errors of $p$	Orders
16	2.119e-3 & 1.020e-1		9.406e-3 & 7.907e-1		1.265e-2 & 2.455e-1	
32	5.175e-4 & 2.572e-2	2.03 & 1.99	2.363e-3 & 3.919e-1	1.99 & 1.01	3.208e-3 & 1.151e-1	1.98 & 1.09
64	1.296e-4 & 6.448e-3	2.00 & 2.00	5.926e-4 & 1.954e-1	2.00 & 1.00	8.063e-4 & 5.581e-2	1.99 & 1.04
128	3.246e-5 & 1.614e-3	2.00 & 2.00	1.483e-4 & 9.764e-2	2.00 & 1.00	2.019e-4 & 2.748e-2	2.00 & 1.02

**Table 9** Rate of convergence of the decoupled algorithm for  $K = 10^{-6}$ .

1/h	$L^2 \& H^1$ errors of $\boldsymbol{u}$	Orders	$L^2 \& H^1$ errors of $\xi$	Orders	$L^2 \& H^1$ errors of $p$	Orders
16	2.120e-3 & 1.020e-1		9.409e-3 & 7.907e-1		1.266e-2 & 2.457e-1	_
32	5.181e-4 & 2.572e-2	2.03 & 1.99	2.364e-3 & 3.919e-1	1.99 & 1.01	3.210e-3 & 1.153e-1	1.98 & 1.09
64	1.298e-4 & 6.448e-3	2.00 & 2.00	5.932e-4 & 1.955e-1	1.99 & 1.00	8.075e-4 & 5.598e-2	1.99 & 1.04
128	3.257e-5 & 1.614e-3	2.00 & 2.00	1.485e-4 & 9.765e-2	2.00 & 1.00	2.024e-4 & 2.760e-2	2.00 & 1.02

stability of the algorithm and the time errors are small enough. From Tables 4 and 5, we see that for all variables, the decoupled algorithm also gives optimal orders of convergence in the energy norm.

By comparing Table 3 with Table 2 (and comparing Table 5 with Table 4), we observe that as the Poisson ratio is approaching 0.49999, the mixed linear elasticity model is closer to the incompressible Stokes model, and therefore the numerical errors for u and  $\xi$  are larger.

#### 3.2. Tests for the parameter K

Another parameter we are interested in is the hydraulic conductivity K. For testing the robustness of our algorithms with respect to K, we fix  $\nu=0.3$  and  $c_0=1$ , while vary K to be  $K=1\times 10^{-6}$  and  $K=1\times 10^{-2}$ . (The case K=1.0 is already reported in Table 2.) Again, we use  $\Delta t=10^{-5}$  for the coupled algorithm, and  $\Delta t=10^{-6}$  for the decoupled algorithm.

Table 6 and Table 7 are based on the coupled algorithm. In these two tables, we display the numerical errors and the convergence rates for  $K = 10^{-2}$  and  $K = 10^{-6}$  respectively. No matter  $K = 10^{-6}$  or  $K = 10^{-2}$ , we see that the errors of all variables are small and the convergence orders are optimal in the energy norm. Comparing Tables 6 and 7 with Table 2, we see that K has a small influence on the errors and the convergence rates. Moreover, it shows clearly that the coupled algorithm is robust with respect to K. For the decoupled algorithm, Table 9 is based on  $K = 10^{-6}$  and Table 8 is based on  $K = 10^{-2}$ . From Tables 8 and 9, we see that the error orders are optimal again in the energy norm, which demonstrate that the decoupled algorithm is robust with respect to the parameter K.

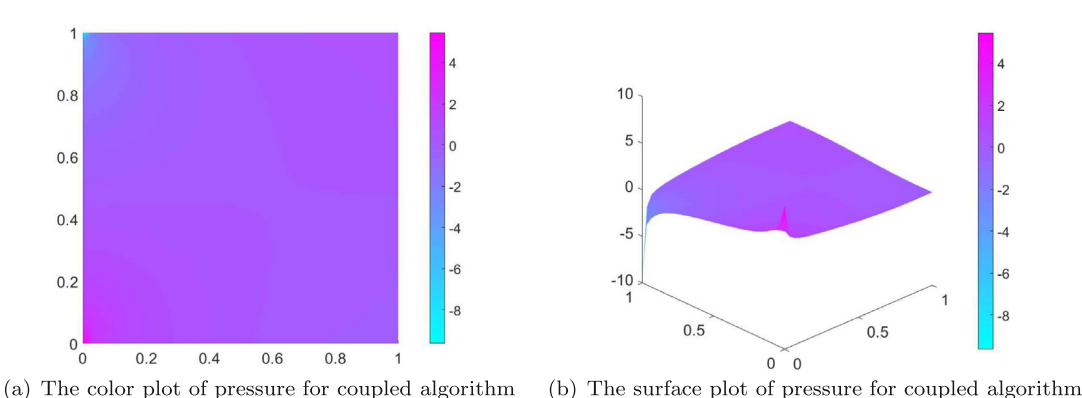


Fig. 2. The pressure distribution for coupled algorithm. (For interpretation of the references to color in this figure legend, the reader is referred to the web version of this article.)

## 3.3. Tests for pressure oscillations

To check whether the algorithms can resolve the pressure oscillation problem in solving Biot model, we consider the cantilever bracket problem [13,39,49]. In our tests, all settings including physical parameters, boundary and initial conditions, and discretization parameters, are the same as those in [13,49]. Specifically, the computational domain and  $\Gamma$  are same as Example 1. The material parameters are  $E=10^5$ ,  $\nu=0.4$ ,  $c_0=0$ ,  $\alpha=1.0$ ,  $K=1\times10^{-7}$ ,  $\Delta t=0.001$ . There is no force term or source term, that is, f=0 and  $Q_s=0$ . The boundary conditions are taken as

$$\begin{split} \nabla p &= 0, & \text{on } \partial \Omega, \\ \pmb{u} &= 0, & \text{on } \Gamma_3 \times (0,T), \\ \sigma \pmb{n} - \alpha p \pmb{n} &= \pmb{h}, & \text{on } \Gamma_j \times (0,T), \ j &= 1,2,4. \end{split}$$
 where  $\pmb{h} = (h_1,h_2)$  with  $h_1 = 0, & \text{on } \Gamma_j, \ j = 1,2,4, \quad \text{and}, \quad h_2 = \left\{ \begin{array}{ll} 0 & \text{on } \Gamma_j \times (0,T), \ j = 1,2,4, \\ -1 & \text{on } \Gamma_4 \times (0,T) \end{array} \right.$ 

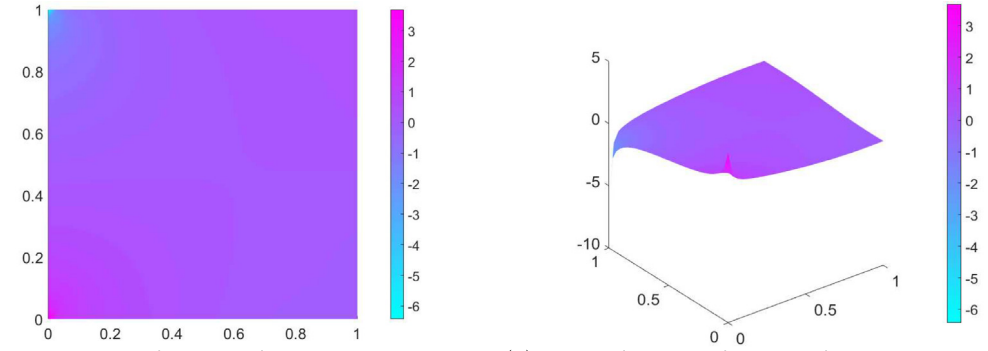
The zero initial conditions are assigned for both u and p [13,49].

For both the coupled and the decoupled algorithm, we let h = 1/32,  $\Delta t = 0.001$ , and run 1 step of time evolution. In Figs. 2 and 3, we display the surface and color plot of the computed pressure based on the two different algorithms. From the results, one can see clearly that the numerical solutions based on the two algorithms do not suffer from the pressure oscillation.

In summary, after performing the tests for the parameters  $\nu$  and K using both the coupled and decoupled algorithms, we observe that no matter how physical parameters vary, error orders of different variables are optimal in the energy norm for the two algorithms. Therefore, they are robust with respect to the physical parameters. The proposed algorithms are also locking free and pressure oscillation free. Locking phenomenon happens when lower order finite elements directly applied to the single linear elasticity operator and the Poisson ratio is close to 0.5. A good remedy is to employ the mixed form of the linear elasticity operator. The algorithms in this paper also follow such a strategy. For pressure oscillation, it is related to the properties of discrete Schur complement. We have numerically verified that the proposed algorithms are oscillation free. The coupled algorithm is more stable because all variables are solved implicitly in each time step. For the decoupled algorithm, the two subproblems are solved separately and each subproblem has much fewer variables involved in. Therefore, it is easier to implement and computationally efficient.

#### 4. Applications in brain edema simulation

In this section, we apply the two developed algorithms to explore brain swelling caused by brain injury. Both of them give almost the same result, we report the simulation result based on the decoupled algorithm. In our



(a) The color plot of pressure for decoupled algorithm (b) The surface plot of pressure for decoupled algorithm

Fig. 3. The pressure distribution for decoupled algorithm. (For interpretation of the references to color in this figure legend, the reader is referred to the web version of this article.)

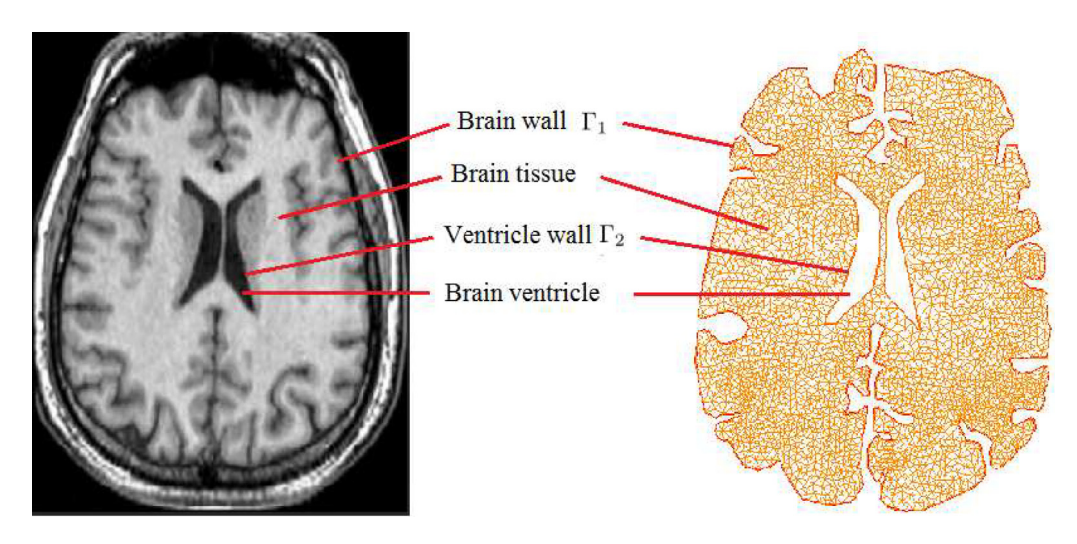


Fig. 4. An MRI slice of a human brain [3] (left) and the FE mesh (right).

simulation, we ignore the influence of gravity and the body force, i.e., g = 0 and f = 0. Besides the governing equations and geometric models, the boundary conditions and relevant parameters are also the vital components in modeling brain edema. We will describe the boundary conditions and investigate the effects of parameters. As mentioned in Section 1, because of the difficulty in measuring the characteristics of brain tissue, there are big variations of the relevant parameters (such as  $c_0$ ,  $\alpha$ , E,  $\nu$ , and K) used in the literature. In order to better understand traumatic brain swelling, we have performed the following two-step procedure. Firstly, we conduct numerical simulations based on the physical parameters used in [25], and set it up as our baseline model. The parameters and the data of the baseline model are validated by comparing our simulation results with the existing published results. Secondly, taking advantage of the parameter robustness of our algorithms, we investigate the effects of those key parameters on brain swelling by comparing our simulation results with the baseline model results. The comparisons are both qualitatively and quantitatively.

The geometry and FE mesh. Our geometric model is a 2D cross-section of a 3D model, see Fig. 4.

In the left part of Fig. 4, a slice of the magnetic resonance imaging (MRI) for a human brain is obtained from [3]. The length and width are 124 mm and 104 mm, respectively. After extracting the geometry, a finite-element mesh of 9155 quasi-uniform triangular elements is generated from the MRI brain atlas by using the GMSH software [15] (see the right part of Fig. 4). As shown in the figure,  $\Gamma_2$  is the ventricular wall whose inner part is the CSF;  $\Gamma_1$  is the brain tissue wall whose outer part is the SAS part.

**Table 10** Parameter values.

Parameters	Values	Parameters	Values
$c_0$	$4.5 \times 10^{-7} \text{ Pa}^{-1}$	κ	$1.4 \times 10^{-9} \text{ mm}^2$
$c_b$	$3 \times 10^{-5}$ mm/min/Pa	α	1
$p_{SAS}$	1070 Pa	ν	0.35
$\mu_f$	$1.48 \times 10^{-5} \text{ Pa} \cdot \text{min}$	E	9010 Pa

BCs and justification. Suitable boundary conditions are described and justified as follows.

•  $\Gamma_1$  is the brain tissue wall which is closed to the skull, so the displacement along  $\Gamma_1$  is zero, i.e.,

$$\boldsymbol{u} = \boldsymbol{0} \quad \text{on } \Gamma_1.$$
 (18)

When CSF flowing out of the brain tissue, it is absorbed by the SAS part. The CSF absorption is linearly dependent on the difference value of the pressure on the brain tissue wall and the pressure of SAS ( $p_{SAS}$ ). The balance of flow rate leads to

$$(K\nabla p) \cdot \mathbf{n} = c_b (p_{SAS} - p) \quad \text{on } \Gamma_1,$$
 (19)

where  $c_b$  is the value of conductance. According to [24,41,46], the ventricular CSF flows out of the ventricle from the aqueduct satisfies Darcy's law. From the data provided in [46], a normal brain will produce (discharge) 0.38 ml/min CSF, and the rate of CSF outflowing from the aqueduct is approximately 0.31 ml/min. This means that the rate of CSF outflows through brain parenchyma is  $Q_0 = 0.07$  ml/min. The conductance  $c_b$  can be calculated by

$$c_b = \frac{Q_0}{p_d A_{SAS}}.$$

Here,  $p_d = 30$  Pa is the difference between the ventricular pressure ( $\approx 1100$  Pa) and  $p_{SAS}$  ( $\approx 1070$  Pa) for a normal person;  $A_{SAS}$  is the surface area of the SAS, approximately equals 76000 mm<sup>2</sup>, which is 1/3 of the area of the cerebral cortex [44]. Therefore, we have  $c_b = 3.0 \times 10^{-5}$  mm/min/Pa.

• On the ventricle wall  $\Gamma_2$ , the total normal force from the tissue part needs to be balanced with the fluid pressure from the ventricle. That is:

$$(\boldsymbol{\sigma} - \alpha \boldsymbol{p}) \cdot \boldsymbol{n} = -\boldsymbol{p} \cdot \boldsymbol{n} \quad \text{on } \Gamma_2. \tag{20}$$

The result of Li et al. in [25] illustrates that the pressure at the ventricle wall is around

$$p = 1100 \text{ Pa}$$
 on  $\Gamma_2$ .

## 4.1. The baseline model and the simulation results

As our first step, we conduct the numerical simulations using a baseline model. The relevant physical parameters are listed in Table 10. For the permeability of brain tissue, we choose  $\kappa = 1.4 \times 10^{-9}$  mm<sup>2</sup>, which is an average of the permeabilities of gray matter and white matter [7]. For the other parameters, their values are chosen to be the same as those used in [25,26]. We list them in Table 10.

Based on the baseline modeling parameters in Table 10, we first conduct the simulation for a brain of normal state. When the brain is in a normal state, CSF's absorption and discharge are in balance, i.e.,  $Q_s = 0$  [41]. There is no deformation for parenchyma while the ventricular pressure is slightly higher than that in SAS, see Fig. 5 for the simulation results of ICP. The pressure distribution lies between 1070–1100 Pa, which is consistent with the fact of pressure distribution in normal brain [1]. Meanwhile, we list the simulation result from [25,27] in Fig. 6. Fig. 6 is a 2D cross sectional image based on a 3D simulation which includes the ventricular pressure distribution (the approximate position is in the hollow part of Fig. 5), brain tissue pressure distribution, and the CSF velocity streamlines (the line part). Comparing brain tissue pressure distribution between Figs. 5 and 6, it is clear that our simulation result is close to that in [25].

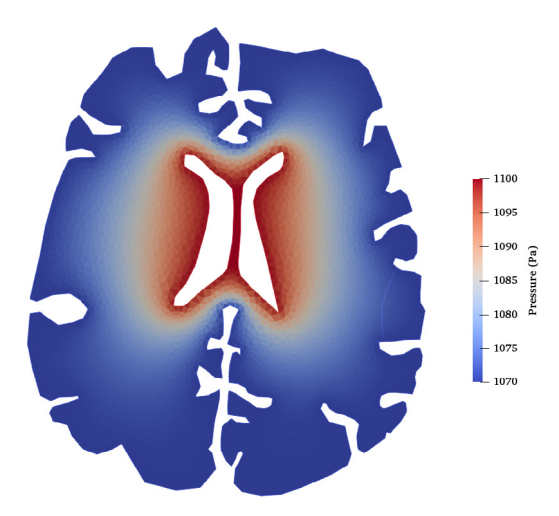
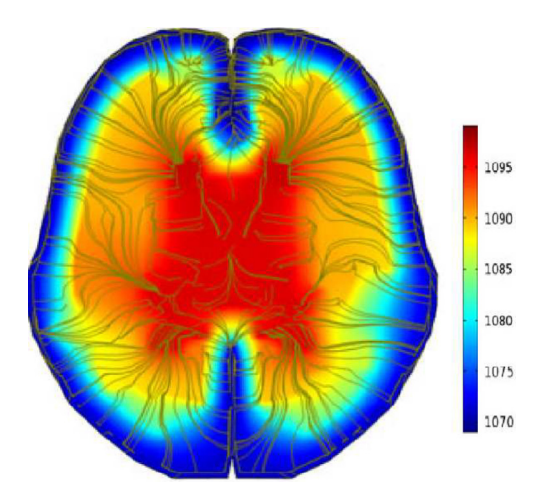


Fig. 5. Pressure distribution of a normal state of brain (our simulation results and physical parameters used in [25]).



**Fig. 6.** Pressure distribution of a normal state brain. *Source:* Picture obtained from [25].

Once TBI happens, the dynamic equilibrium of absorption and discharge could be broken easily. The injured part will absorb the CSF, which causes the deformation of brain tissue and local increased ICP. Meanwhile, the brain tissue will squeeze the ventricle because of the fixed skull. For simulating the brain edema after TBI, the brain tissue is divided into two parts: the normal part  $\Omega_n$  (8989 triangular elements) and the injured part  $\Omega_i$  (166 triangular elements), see Fig. 7 for an illustration. According to the experimental data in [25,26,40], the pressure difference between the swelling area and the normal area of the brain is 15 mmHg ( $\approx 2000$  Pa), which means that the pressure on the injured area approximately equals 3000 Pa. Moreover, the pressure difference linearly depends on the absorption rate  $Q_s$ . Using this information, we obtain the maximum ICPs under different absorption rates (see Fig. 8). From Fig. 8, we observe that the peak value of our ICP matches the maximum pressure values reported in [25,40] when  $Q_s = 9 \times 10^{-3}$  /min. Therefore, we set  $Q_s = 9 \times 10^{-3}$  /min in  $\Omega_i$  in our brain swelling simulation. For other physical parameters, as we have validated them for the normal state simulations, we continue to use the values listed in Table 10

Based on the data discussed above, we present the ICP and brain tissue displacement distribution for an injured brain in Fig. 9. The maximum pressure,  $p_{max}$ , in the injured area is 3025 Pa. This is consistent with that in [25]. Influenced by the total stress, the brain tissue in the swelling area deforms and compresses the surrounding brain

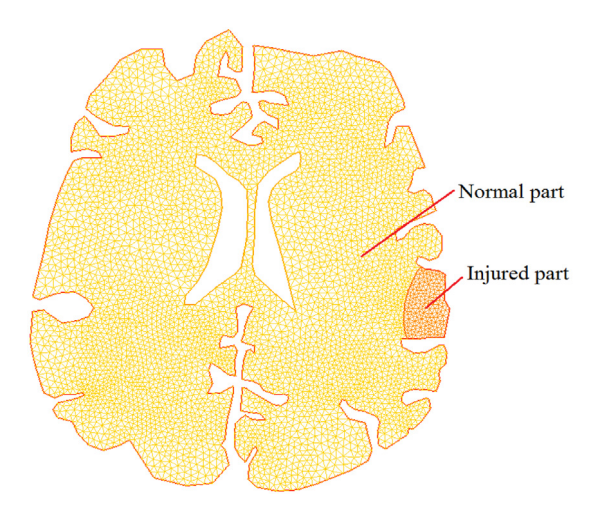


Fig. 7. The FE mesh for a brain with an injured region.

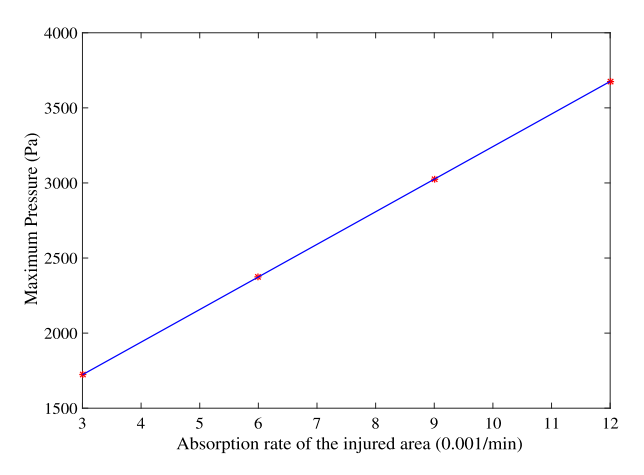


Fig. 8. The maximum values of ICP under different absorbing rates.

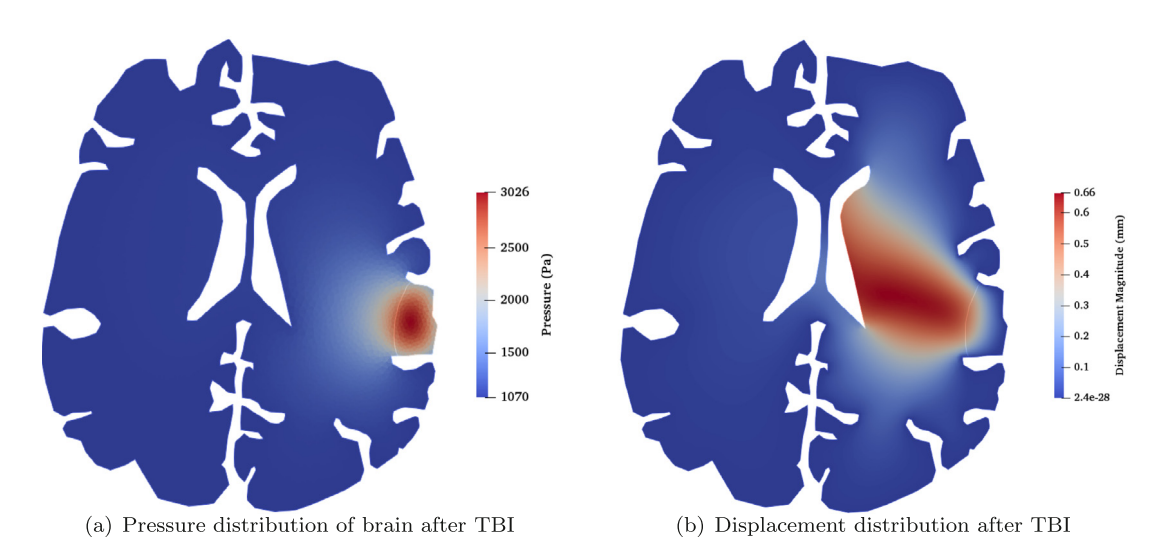


Fig. 9. Pressure and displacement distribution after TBI.

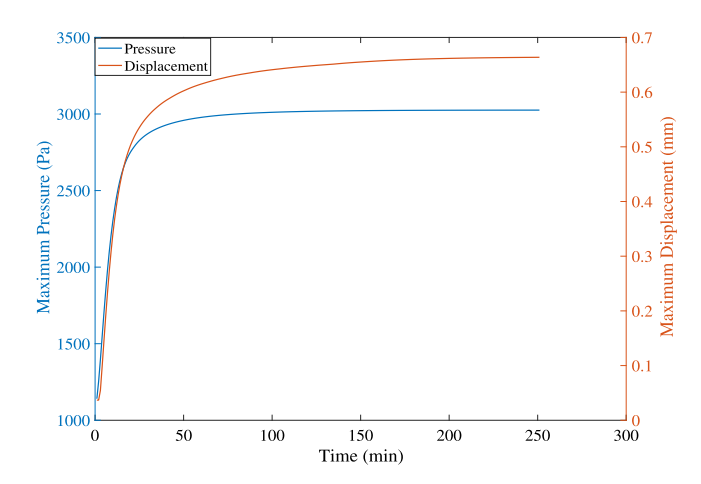


Fig. 10. The maximum values of ICP and tissue displacement as time evolves after TBI (parameters are from the baseline model).

**Table 11** The maximum values of u and p ( $u_{max}$  and  $p_{max}$ ) under different values of E. Fixing  $v = v_0$  and  $\kappa = \kappa_0$ .

	$\mu$	$1/\lambda$	$u_{max}$	$p_{max}$
$E = 0.2E_0$ $E = 2E_0$	667 Pa	$6.42 \times 10^{-4} \text{ Pa}^{-1}$	3.3 mm	3023 Pa
	6674 Pa	$6.42 \times 10^{-5} \text{ Pa}^{-1}$	0.332 mm	3025 Pa

tissue. Because the skull is fixed and the ventricle is free, brain tissue deformation moves toward the ventricle. In our simulation, the maximum tissue deformation,  $u_{max}$ , is 0.664 mm.

In Fig. 10, we plot the maximum values of pressure and tissue deformation as functions of time. From the figure, we see that the values of the maximum ICP and the tissue deformation increase rapidly in the first hour. Then, the increasing speeds slow down. At around 4.2 h, both the ICP and the tissue deformation reach their peak values. This phenomenon is in line with the biomedical observation in [11,40] and consistent with the results in [25,26].

#### 4.2. The effects of key physical parameters

To have a better understanding of brain swelling, we investigate the effects of the key physical parameters using the model of Section 4.1. Here, we consider three key parameters: E,  $\nu$ , and  $\kappa$ . When testing one parameter, we fix the other values to be the same as those in the baseline model listed in Table 10, i.e., each parameter is modified independently from the otherwise baseline values (For the ease of notations, we set the baseline model parameters to be:  $E_0 = 9010 \text{Pa}$ ,  $\nu_0 = 0.35$ , and  $\kappa_0 = 1.4 \times 10^{-9} \text{ mm}^2$ ). The parameter values of each test are listed in Tables 11–13, respectively. We only plot the maximum values of ICP and brain tissue displacement as functions of time, because the distributions of displacement and pressure are similar to those of the baseline model, we skip their plots here.

In Table 11 and Fig. 11, we present the effects of Young's modulus E on the values of  $u_{max}$  and  $p_{max}$ . Young's modulus E refers to the stiffness of a material. The larger E is, the smaller the tissue deformation is. From Table 11, we observe that when the Young's modulus E are  $0.2E_0$  and  $2E_0$ ,  $u_{max}$  equal to 3.3 mm and 0.332 mm respectively, which are 4.97 and 0.5 times of the baseline value (= 0.664 mm). From Table 11, we also observe that the change of E has small effects on the pressure value. However, Fig. 11 illustrates that when Young's modulus ranges from  $0.2E_0$  to  $2E_0$ , the total developing time are 909 and 140 min, respectively, which are 3.61 and 0.56 times of that for the baseline model. This means that it has a big influence on the swelling speed. Larger E will make brain swelling develops much faster than expected.

In Table 12 and Fig. 12, we present the effects of the Poisson ratio v on the values of  $u_{max}$  and  $p_{max}$ . Poisson ratio measures how incompressible a material is. In Table 12, we let Poisson ratio ranges from 0.3 and 0.496 (the value derived in [14]). The corresponding  $u_{max}$  values are 1.11 and 0.07 times of that in baseline model (= 0.664 mm). When the Poisson ratio is approaching to 0.5, one obtains a very small  $u_{max}$ , which means the brain tissue is nearly

Table 12 The maximum values of u and p ( $u_{max}$  and  $p_{max}$ ) under different values of v. Fixing  $E = E_0$  and  $\kappa = \kappa_0$ .

	μ	1/λ	$u_{max}$	$p_{max}$
$\nu = 0.3$	3465 Pa	$1.9 \times 10^{-4} \text{ Pa}^{-1}$	0.7356 mm	3025 Pa
v = 0.496	3011 Pa	$2.68 \times 10^{-6} \text{ Pa}^{-1}$	0.04652 mm	3025 Pa

Table 13 The maximum values of u and p ( $u_{max}$  and  $p_{max}$ ) under different values of  $\kappa$ . Fixing  $E = E_0$  and  $\nu = \nu_0$ .

	$\mu$	$1/\lambda$	$u_{max}$	$p_{max}$
$\kappa = 0.1\kappa_0$	3337 Pa	$1.28 \times 10^{-4} \text{ Pa}^{-1}$	3.537 mm	13805 Pa
$\kappa = 10\kappa_0$	3337 Pa	$1.28 \times 10^{-4} \text{ Pa}^{-1}$	0.2232 mm	1619 Pa

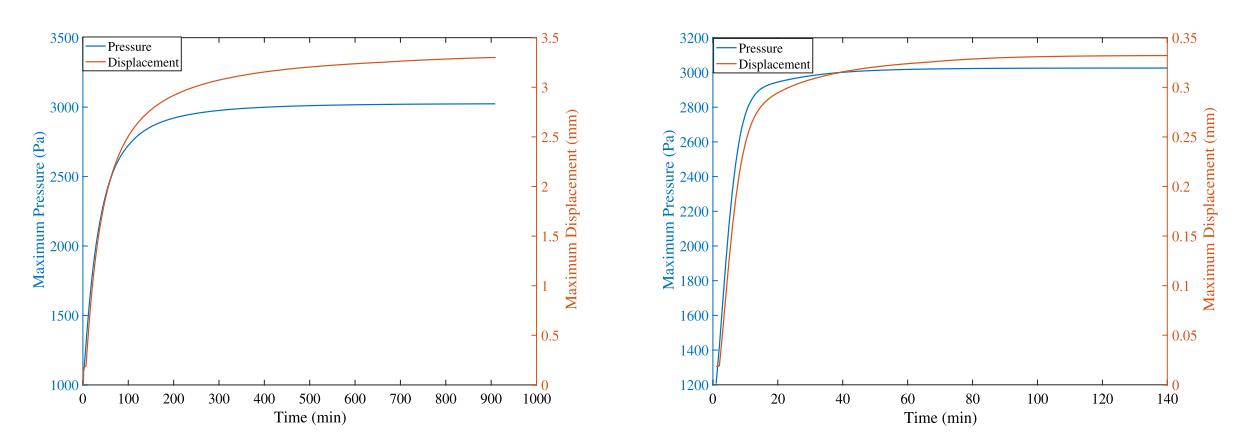


Fig. 11. The maximum values of pressure and displacement as time evolves.  $E = 0.2E_0$  (left),  $E = 2E_0$  (right).

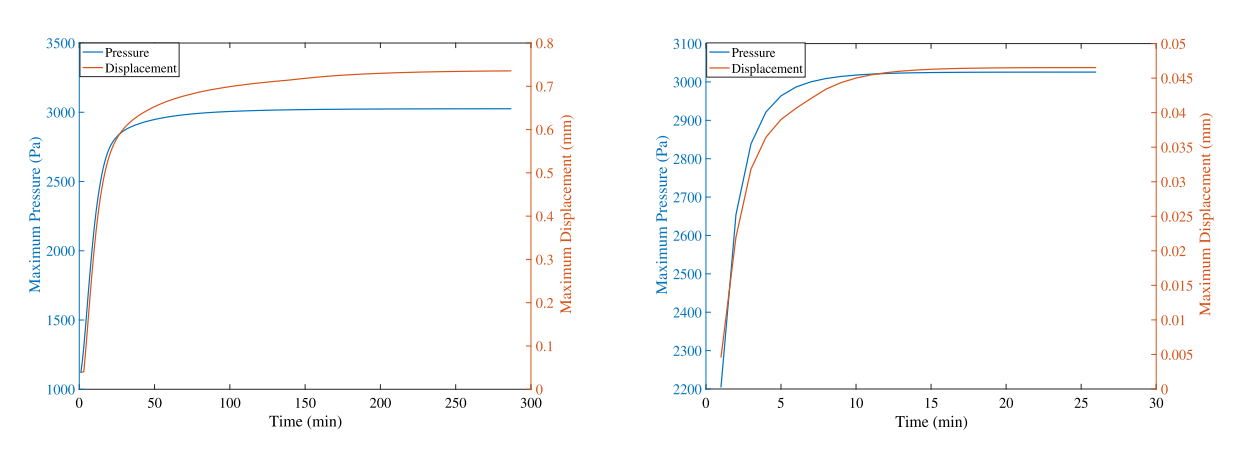


Fig. 12. The maximum values of pressure and displacement as time evolves.  $\nu = 0.3$  (left),  $\nu = 0.496$  (right).

incompressible. Meanwhile, the peak values of ICP almost have no change. From Fig. 12, the total developing time corresponding to  $\nu = 0.3$  and 0.496 is 286 and 26 min respectively, which is 1.138 and 0.103 times that of the baseline model. Similar to the effects of the Young's modulus E, larger Poisson ratio will make brain swelling develops much faster.

In Table 13 and Fig. 13, we show the effects of  $\kappa$  on the values of  $u_{max}$  and  $p_{max}$ . Table 13 shows that when the testing permeability  $\kappa$  is 0.1  $\kappa_0$  (or 10  $\kappa_0$ ), the  $u_{max}$  is 532% (or 33.6%) of that in the baseline value (= 0.664 mm), while  $p_{max}$  is 456% (or 53.5%) times of the baseline value (= 3025 Pa). Meanwhile, the developing times for the two cases are 25 h and 51 min, which are 5.95 and 0.202 times that of the baseline model respectively. Unlike the Poisson ratio  $\nu$  and the Young's modulus E, which only affect the tissue deformation, permeability  $\kappa$  has a

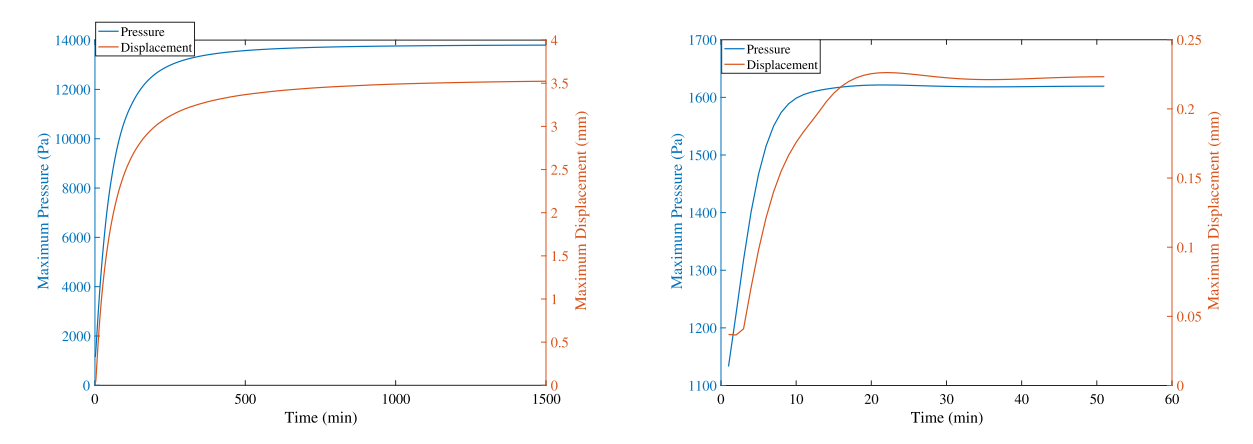


Fig. 13. The maximum values of pressure and displacement as time evolves.  $\kappa = 0.1\kappa_0$  (left),  $\kappa = 10\kappa_0$  (right).

big influence on both  $u_{max}$  and  $p_{max}$ . A lower permeability will result in higher pressure and larger deformation, and therefore will make brain edema more severe. However, higher permeability will make brain swelling develops much faster.

From these Tables and figures, we observe that Young's modulus E and Poisson ratio  $\nu$  have big influence on the value of  $u_{max}$  but small influence on the value of  $p_{max}$ , while  $\kappa$  has big influences on both of them. Moreover, we conclude that larger values of the parameters E,  $\nu$ ,  $\kappa$  will result in a smaller total developing time.

#### 4.3. Discussion

The brain is the most complex and least understood organ in human body. Modeling the brain as a whole virtually impossible with current technology. In this work, we try to apply poroelastic model and the corresponding numerical simulations to study the mechanical aspect of brain edema. Our simulations are based on a 2D geometry. The geometric simplification makes our simulation not as accurate as those 3D simulations. Compared with 3D simulations, the 2D model has some difficulties in simulating the absorption of CSF. To overcome this difficulty, we assume that CSF is absorbed when it seeps from brain tissue to the SAS area. Another limitation of this work is that we use homogenized material properties in our simulations. Brain tissue is actually very complicated and consists of several comparts. These different comparts possess different material properties. For improving the simulation accuracy, multiple network poroelastic model might be a good remedy.

#### 5. Conclusions

In this paper, we develop numerical algorithms for the Biot model based on a multiphysics reformulation. By introducing an intermediate variable, the Biot equations are written into a system of a generalized Stokes problem and a reaction-diffusion problem. To solve this system, a coupled algorithm and a decoupled algorithm are developed. The approximation accuracy of the algorithms is examined by testing a benchmark problem under different settings of physical parameters. It is shown that the approximation accuracies of the two algorithms are robust with respect to the parameters.

For simulating brain edema, we firstly compare the results with the existing work to validate our model and data. Our simulation results show good agreement with the biomedical observations and the numerical results presented in [25,26,33,34]. Then, we carefully investigate the effects of each key parameters. Base on the simulation results, we conclude that (i) The values of E and  $\nu$  will not affect the maximum values of ICP (but will affect the maximum values of tissue displacement). (ii) The permeability has the greatest impact on both the max ICP and the max tissue deformation; Low permeability will make brain edema more severe; (iii) Increasing E,  $\nu$ , and  $\kappa$  will make brain swelling develops faster.

### Acknowledgments

The authors would like to thank the two anonymous reviewers for giving them many valuable suggestions which substantially improved the quality of this paper.

#### References

- [1] M. Albeck, S. Børgesen, F. Gjerris, J. Schmidt, P. Sørensen, Intracranial pressure and cerebrospinal fluid outflow conductance in healthy subjects, J. Neurosurg. 74 (4) (1991) 597–600.
- [2] Intracranial hypertension. https://ihrfoundation.org/hypertension/info/C16.
- [3] http://www.med.harvard.edu/aanlib/cases/caseNA/pb9.htm.
- [4] M.A. Biot, General theory of three-dimensional consolidation, J. Appl. Phys. 12 (1941) 155-164.
- [5] M.A. Biot, Theory of elasticity and consolidation for a porous anisotropic solid, J. Appl. Phys. 26 (1955) 182–185.
- [6] F. Brezzi, M. Fortin, Mixed and Hybrid Finite Element Methods. Vol. 15, Springer Science & Business Media, 2012.
- [7] S. Budday, R. Nay, R. de Rooij, P. Steinmann, T. Wyrobek, T. Ovaert, E. Kuhl, Mechanical properties of gray and white matter brain tissue by indentation, J. Mech. Behav. Biomed. Mater. 46 (2015) 318–330.
- [8] M. Cai, Analysis of some projection method based preconditioners for models of incompressible flow, Appl. Numer. Math. 90 (2015) 77–90.
- [9] M. Cai, L. Pavarino, O. Widlund, Overlapping Schwarz methods with a standard coarse space for almost incompressible linear elasticity, SIAM J. Sci. Comput. 37 (2) A811–A831.
- [10] M. Cai, G. Zhang, Comparisons of some iterative algorithms for Biot equations, Int. J. Evol. Equ. 10 (3–4) (2017) 267–282, a special issue Differential Equations, Almost Periodicity, and Almost Automorphy, dedicated to the memory of Prof. V.V. Zhikov.
- [11] Y. Chen, J. Guan, To explore the mechanism of death after loosening the body into a buckling position, J. Lanzhou Univ. Med. Ed. (1) (2005) 2 (In Chinese).
- [12] C. Dohrmann, O. Widlund, An overlapping Schwarz algorithm for almost incompressible elasticity, SIAM J. Numer. Anal. 47 (4) (2009) 2897–2923.
- [13] X. Feng, Z. Ge, Y. Li, Analysis of a multiphysics finite element method for a poroelasticity model, IMA J. Numer. Anal. 38 (2018) 330–359.
- [14] G. Franceschini, D. Bigoni, P. Regitnig, G. Holzapfel, Brain tissue deforms similarly to filled elastomers and follows consolidation theory, J. Mech. Phys. Solids 54 (12) 2592-2620.
- [15] C. Geuzaine, J. Remacle, GMSH: A three-dimensional finite element mesh generator with built-in pre- and post-processing facilities, Internat. J. Numer. Methods Engrg. 79 (11) (2009) 1309–1331.
- [16] M. Griebel, D. Oeltz, M. Schweitzer, An algebraic multigrid method for linear elasticity, SIAM J. Sci. Comput. 25 (2) (2003) 385–407.
- [17] S. Hakim, J. Venegas, J. Burton, The physics of the cranial cavity, hydrocephalus and normal pressure hydrocephalus: mechanical interpretation and mathematical model, Surg. Neurol. 5 (3) (1976) 187–210.
- [18] F. Hecht, New development in FreeFem++, J. Numer. Math. 20 (3-4) (2012) 251-266.
- [19] J. Kim, H.A. Tchelepi, R. Juanes, Stability and convergence of sequential methods for coupled flow and geomechanics: Drained and undrained splits, Comput. Methods Appl. Mech. Engrg. 200 (23–24) (2011) 2094–2116.
- [20] J. Korsawe, G. Starke, A least-squares mixed finite element method for Biot's consolidation problem in porous media, SIAM J. Numer. Anal. 43 (2005) 318–339.
- [21] J. Korsawe, G. Starke, W. Wang, O. Kolditz, Finite element analysis of poro-elastic consolidation in porous media: standard and mixed approaches, Comput. Methods Appl. Mech. Engrg. 195 (2006) 1096–1115.
- [22] J.J. Lee, Robust error analysis of coupled mixed methods for Biot's consolidation model, J. Sci. Comput. 69 (2016) 610-632.
- [23] J.J. Lee, K.A. Mardal, R. Winther, Parameter-robust discretization and preconditioning of Biot's consolidation model, SIAM J. Sci. Comput. 39 (1) (2017) A1–A24.
- [24] D. Levine, The pathogenesis of normal pressure hydrocephalus: a theoretical analysis, Bull. Math. Biol. 61 (5) (1999) 875-916.
- [25] X. Li, H. von Holst, S. Kleiven, Influence of gravity for optimal head positions in the treatment of head injury patients, Acta Neurochir. (Wien) 153 (10) (2011) 2057–2064.
- [26] X. Li, H. von Holst, S. Kleiven, Decompressive craniectomy causes a significant strain increase in axonal fiber tracts, J. Clin. Neurosci. 20 (4) (2013) 509–513.
- [27] X. Li, H. von Holst, S. Kleiven, Influences of brain tissue poroelastic constants on intracranial pressure (ICP) during constant-rate infusion, Comput. Methods Biomech. Biomed. Eng. 16 (12) (2013) 1330–1343.
- [28] A. Linninger, B. Sweetman, R. Penn, Normal and hydrocephalic brain dynamics: the role of reduced cerebrospinal fluid reabsorption in ventricular enlargement, Ann. Biomed. Eng. 37 (7) (2009) 1434–1447.
- [29] A. Marmarou, Pathophysiology of traumatic brain edema: current concepts, in: Brain Edema XII, Springer, Vienna, 2003, pp. 7-10.
- [30] M. Miga, K. Paulsen, P. Hoopes, In vivo modeling of interstitial pressure surgical load using finite elements, Trans. ASME 122 (2000) 354–363.
- [31] M.A. Murad, A.F.D. Loula, On stability and convergence of finite element approximations of Biot's consolidation problem, Internat. J. Numer. Methods Engrg. 37 (1994) 645–667.
- [32] M.A. Murad, V. Thomée, A.F.D. Loula, Asymptotic behavior of semidiscrete finite-element approximations of Biot's consolidation problem, SIAM J. Numer. Anal. 33 (1996) 1065–1083.
- [33] T. Nagashima, T. Norihiko, M. Satoshi, H. Barry Horwitz, S. Yasuyuki, Biomechanics of hydrocephalus: a new theoretical model, Neurosurgery 21 (6) (1987) 898–904.

- [34] T. Nagashima, T. Shirakuni, S. Rapoport, A two-dimensional, finite element analysis of vasogenic brain edema, Neurol. Med. Chir. 30 (1) (1990) 1–9.
- [35] T. Nagashima, N. Tamaki, T. Shirakuni, S. Matsumoto, Y. Seguchi, T. Tamura, Biomechanics of vasogenic brain edema application of Biots consolidation theory and the finite element method, in: Brain Edema, Springer, Berlin, Heidelberg, 1985, pp. 92–98.
- [36] A. Naumovich, On finite volume discretization of the three-dimensional biot poroelasticity system in multilayer domains, Comput. Methods Appl. Math. 6 (3) (2006) 306–325.
- [37] R. Oyarzùa, R. Ruiz-Baier, Locking-free finite element methods for poroelasticity, SIAM J. Numer. Anal. 54 (5) (2016) 2951-2973.
- [38] P.J. Phillip, M.F. Wheeler, Overcoming the problem of locking in linear elasticity and poroelasticity: an heuristic approach, Comput. Geosci. 13 (2009) 5–12.
- [39] P.J. Phillips, M.F. Wheeler, A coupling of mixed and continuous Galerkin finite element methods for poroelasticity I: the continuous in time case, Comput. Geosci. 11 (2007) 131–144.
- [40] H.J. Reulen, H.G. Kreysch, Measurement of brain tissue pressure in cold induced cerebral oedema, Acta Neurochir. 29 (1–2) (1973)
- [41] A. Smillie, I. Sobey, Z. Molnar, A hydroelastic model of hydrocephalus, J. Fluid Mech. 539 (2005) 417-443.
- [42] J.H. Smith, J.A. Humphrey, Interstitial transport and transvascular fluid exchange during infusion into brain and tumor tissue, Microvasc. Res. 73 (1) (2007) 58–73.
- [43] Z. Taylor, K. Miller, Reassessment of brain elasticity for analysis of biomechanisms of hydrocephalus, J. Biomech. 37 (8) (2004) 1263–1269.
- [44] R. Toro, M. Perron, B. Pike, L. Richer, S. Veillette, Brain size and folding of the human cerebral cortex, Cerebral cortex 18 (10) (2008) 2352–2357.
- [45] S. Turek, Efficient Solvers for Incompressible Flow Problems: An Algorithmic and Computional Approach. vol. 6, Springer Verlag, 1999.
- [46] J.C. Vardakis, D. Chou, B.J. Tully, C.C. Hung, T.H. Lee, P.H. Tsui, Y. Ventikos, Investigating cerebral oedema using poroelasticity, Med. Eng. Phys. 38 (1) (2016) 48–57.
- [47] S.Y. Yi, A coupling of nonconforming and mixed finite element methods for Biot's consolidation model, Numer. Methods Partial Differential Equations 29 (2013) 1749–1777.
- [48] S.Y. Yi, Convergence analysis of a new mixed finite element method for Biot's consolidation model, Numer. Methods Partial Differential Equations 30 (2014) 1189–1210.
- [49] S.Y. Yi, A study of two modes of locking in poroelasticity, SIAM J. Numer. Anal. 55 (2017) 1915–1936.
- [50] S. Yi, M.L. Bean, Iteratively coupled solution strategies for a four-field mixed finite element method for poroelasticity, Int. J. Numer. Anal. Methods Geomech. 41 (2) (2017) 159–179.
- [51] O.C. Zienkiewicz, T. Shiomi, Dynamic behaviour of saturated porous media; the generalized Biot formulation and its numerical solution, Internat. J. Numer. Anal. Methods Geomech. 8 (1984) 71–96.